

High-throughput calculations of spintronic
tetra-phase transition metal dinitrides†Cite this: *J. Mater. Chem. C*, 2021,
9, 14401Junfei Ding,^a Qiushi Yao,^b Huasheng Sun,^a Shanbao Chen,^{id}^a Fang Wu,^{id}^c
Chengxi Huang^{id}*^a and Erjun Kan^{id}*^a

Two-dimensional (2D) transition metal dinitrides (TMN₂) have attracted increasing attention owing to their diverse geometry configurations and versatile properties. Because of the large electrostatic repulsion between highly charged N³⁻ ions, TMN₂ could show a low-coordination-number geometry different from transition metal dichalcogenides (e.g. MoS₂), which would bring about high-temperature ferromagnetism and other unique properties. In this study, we systemically investigated the possible h-, t- and novel tetra-phases of 2D TMDNs (TM = all the 3d, 4d and 5d transition metals) via high-throughput first-principles calculations. The results show that the 2D tetra-phases for several systems are energetically preferred than their h- and t-phases. These 2D tetra-phases are dynamically and thermally stable with comparable mechanical properties to 2D MoS₂ and germanene. Tetra-MoN₂ and tetra-WN₂ are semiconductors, while tetra-TcN₂, tetra-RuN₂, tetra-ReN₂, tetra-OsN₂ and tetra-IrN₂ are metals. In particular, tetra-MnN₂ exhibits ferromagnetic half-metallicity with a Curie temperature (*T_c*) of up to ~360 K and out-of-plane magnetic anisotropy. These findings expand the family of 2D TMN₂ and provide a material database for future theoretical and experimental studies on 2D spintronic materials.

Received 7th August 2021,
Accepted 14th September 2021

DOI: 10.1039/d1tc03700e

rsc.li/materials-c

Introduction

Two-dimensional (2D) van der Waals (vdW) ferromagnetic materials have been recognized as a cutting-edge topic^{1–4} since they not only provide opportunities to revolutionize the development of spintronic devices⁵ but also serve as a testbed for the study of different aspects of 2D magnetism.^{6,7} Many exotic phenomena (such as current induced magnetic switching in few-layer Fe₃GeTe₂⁸) and excellent performances (such as the giant magnetoresistance in spin-filtered magnetic vdW heterojunctions⁹) of these vdW magnets have also been observed in spintronic devices. However, most of the reported vdW spintronic devices function at temperatures far below the room temperature, which hinders their further practical applications. Thus, the search for 2D vdW materials with high abundance, long spin lifetime, easy manipulation of spin current, and temperature resistivity of spin properties is highly desired.⁵

In the past decade, many studies have been devoted to 2D magnetism, such as the research on transition metal chalcogenides

(TMDs) and halides (TMHs) (e.g. VSe₂,¹⁰ CrTe₂,¹¹ CrSBr¹² and CrX₃¹³), and even high-throughput calculations^{14,15} were performed to find new 2D magnetic materials, while transition metal nitrides were rarely mentioned. Recently, since the bulk layered structure of MoN₂ was experimentally synthesized,¹⁶ many theoretical efforts have been devoted to the investigation of the stable phases and the corresponding properties of 2D transition metal dinitride (2D-TMN₂) sheets.^{17–19} Hexagonal bilayer NbN₂ was predicted as a metal with intra- and inter-layer ferromagnetic couplings.²⁰ Hexagonal monolayer HfN₂ was theoretically reported as a semiconductor with a direct band gap and it also exhibits large valley spin splitting.^{21–23} The trigonal prismatic structure (h-phase) of the MoN₂ (h-MoN₂) monolayer was predicted theoretically to have a robust ferromagnetism with a Curie temperature over 420 K²⁴ and its magnetic coupling can be changed from ferromagnetic to antiferromagnetic by applied strain.²⁵ However, further research showed that surface hydrogenation²⁶ is required to maintain the dynamical stability of h-MoN₂. On the other hand, the tetragonal lattice (tetra-phase) of MoN₂²⁷ is predicted to have a much lower energy than the h-phase and octahedral (t-phase) structures.²⁸ Similarly, the ReN₂ monolayer also shows a tetra-phase which is dynamically and mechanically stable and is a superior sodium-ion battery material due to its metallic features.²⁹ Furthermore, the stability of tetra-phase is also confirmed in VN₂ (tetra-VN₂), which has been reported with an excellent electronic conductivity and can be used as a potential electrode material for rechargeable alkali ion batteries.³⁰

^a MIT Key Laboratory of Semiconductor Microstructure and Quantum Sensing and Department of Applied Physics, Nanjing University of Science and Technology, Nanjing 210094, P. R. China. E-mail: ekan@njust.edu.cn, chuanguang@njust.edu.cn

^b Department of Physics, Southern University of Science and Technology, Shenzhen 518055, Guangdong, P. R. China

^c College of Information Science and Technology, Nanjing Forestry University, Nanjing, Jiangsu 210037, P. R. China

† Electronic supplementary information (ESI) available. See DOI: 10.1039/d1tc03700e

From the discovery of an unconventional tetra-phase in TMN₂, it can be understood that, compared with chalcogen and halogen ions (e.g. S²⁻ and Cl⁻), the N³⁻ ion is highly charged in TMDNs, leading to a large interligand electrostatic repulsion. Therefore, TMDNs could exhibit a geometry with a lower coordination number (i.e. 4) than TMDs or TMHs (i.e. 6). More importantly, it is demonstrated that a smaller crystal field splitting could lead to a stronger ferromagnetic coupling.³¹ A lower coordination number usually leads to a smaller crystal field splitting. Thus, it is expected that tetra-phase TMN₂ could show a stronger ferromagnetism than the h- and t-phases.

Inspired by these results, in this study, based on density functional theory (DFT), we systemically investigated the possible h-, t- and tetra-phases of 2D TMDNs (TM = all the 3d, 4d and 5d transition metals). We perform this search starting from constructing the h-, t- and tetra-phases of TMN₂ (87 structures in total) using our custom code. Then we use DFT methods to calculate their lattice constants and energies and obtain a portfolio of 8 tetra-phase structures (i.e., tetra-Mn/Mo/Tc/Ru/W/Re/Os/IrN₂) which are lower in energy than their corresponding h- and t-phases and are dynamically, thermally and mechanically stable. Finally, our further DFT calculation results show that tetra-MoN₂ and tetra-WN₂ are semiconductors with indirect band gaps of 1.38 and 1.96 eV (at the HSE06 level), respectively. Tetra-TcN₂, RuN₂, ReN₂, OsN₂ and IrN₂ are intrinsic metals. In particular, tetra-MnN₂ exhibits ferromagnetic half-metallicity with a Curie temperature (*T_c*) of up to ~360 K and out-of-plane magnetic anisotropy, which indicate that the tetra-MnN₂ monolayer could be a promising material for room temperature nanoscale spintronic applications.

Computational methods

Structural relaxation, total energy and the corresponding electronic property calculations are implemented in the Vienna Ab initio Simulation Package (VASP).³² The projector augmented wave (PAW) method is used to treat the interactions between ion cores and valence electrons.³³ In most cases, the exchange correlation potential is treated using the Perdew–Burke–Ernzerhof (PBE) functional within generalized gradient approximation (GGA),³⁴ and the effective Hubbard *U*_{eff} values of 3, 2, and 1 eV are chosen to describe the Hubbard correction for 3d, 4d, and 5d transition metals, respectively. Specifically, the HSE06 hybrid functional³⁵ is employed to obtain the accurate electronic structures of tetra-MnN₂, tetra-MoN₂ and tetra-WN₂. The energy cutoff and convergence criteria for energy and force are set to be 500 eV, 10⁻⁵ eV, and 0.01 eV Å⁻¹, respectively. 11 × 11 × 1 and 17 × 17 × 1 *K*-point grids are adopted for the optimization and total energy calculations of the structures, respectively. During the geometry optimizations, both the lattice constants *a* and *b*, and the atomic positions were fully relaxed. A vacuum distance of over 15 Å is used to eliminate the interaction between adjacent cells in the vertical orientation. For the tetra-MnN₂ magnetism calculation, the initial magnetic moments for N atoms are set as 0 μ_B in both ferromagnetic

(FM) and antiferromagnetic (AFM) orders; for the Mn atoms, all of them are set as 1 μ_B in the FM order, while in the AFM order half of them (namely the spin-down atoms) are set as -1 μ_B.

The phonon dispersions of the structures are calculated by adopting the PHONOPY package³⁶ and their thermal stability is confirmed by *ab Initio* molecular dynamics (AIMD) simulations. Open source software VASPKIT,³⁷ Matplotlib³⁸ and VESTA³⁹ were used to address and visualize the VASP output files.

Results and discussion

Tetra-TMN₂ and its stability

The tetra-TMN₂ monolayers belong to the space group *P* $\bar{4}$ *M*2 with each transition metal atom being coordinated with 4 nitrogen atoms. We compared the total energy of the h-TMN₂, t-TMN₂ and tetra-TMN₂ structures of each transition metal element in the 3, 4 and 5d period table (totally produced 87 structures and the energy values are listed in Table 1) and found that the tetra-phases of Mn, Mo, Tc, Ru, W, Re, Os and Ir have lower energies (for convenience, we use the term tetra-TMN₂s specifically to denote these total 8 stable structures).

In Fig. 1(a–c) we displayed the optimized structures of tetra-, h-, and t-MnN₂ monolayers, and the corresponding structural parameters marked in Fig. 1(a) are shown in Table 1. The optimized lattice constant (and M–N bond length) of tetra-TMN₂s ranges from 2.97 Å (and 1.77 Å) for tetra-MnN₂ to 3.22 Å (and 1.88 Å) for tetra-WN₂, respectively. Zhang²⁷ *et al.* reported that the lattice constant and M–N bond length of tetra-MoN₂ are 3.22 Å and 1.88 Å, respectively. Liu²⁹ *et al.* reported that these two parameters of tetra-ReN₂ are 3.178 Å and 1.87 Å, respectively. As presented in Table 1, our structural parameters are well consistent with these results. To confirm the energetic stability of tetra-TMN₂s, the cohesive energy was calculated using the formula:

$$E_{\text{coh}} = -(E_{\text{MN}} - E_{\text{M}} - 2E_{\text{N}})/3$$

where, *E*_{MN}, *E*_M and *E*_N are the total energies of tetra-TMN₂s and isolated M and N atoms from the spin-polarized calculations, respectively. The calculated *E*_{coh} of tetra-TMN₂s, as listed in Table 1, ranges from 3.78 eV for tetra-MnN₂ to 5.89 eV for tetra-WN₂. The reported *E*_{coh} values of tetra-VN₂,³⁰ tetra-silicene,⁴⁰ black phosphorene⁴¹ and MoS₂⁴² are 5.03, 3.90, 3.48 and 5.05 eV, respectively. Our values of tetra-TMN₂s are comparable

Table 1 Structural parameters, lattice parameters (*a*), metal–nitride bond lengths (*L*_{M–N}), angles between neighboring bonds (θ_1 , θ_2), cohesive energies (*E*_{coh}) and charge differences on each ligand for Bader analysis

	<i>a</i> = <i>b</i> (Å)	<i>L</i> _{M–N} (Å)	θ_1 (°)	θ_2 (°)	<i>E</i> _{coh} (eV)	Bader (<i>e</i>)
MnN ₂	2.97	1.77	114.50	107.01	3.78	-1.40
MoN ₂	3.22	1.88	117.48	105.62	5.74	-1.88
TcN ₂	3.12	1.84	115.85	106.39	4.96	-1.56
RuN ₂	3.10	1.85	113.40	107.51	4.81	-1.28
WN ₂	3.22	1.88	117.24	105.73	5.89	-2.16
ReN ₂	3.19	1.87	117.34	105.68	5.88	-1.82
OsN ₂	3.13	1.87	114.08	107.22	4.94	-1.52
IrN ₂	3.18	1.88	115.77	106.45	4.37	-1.26

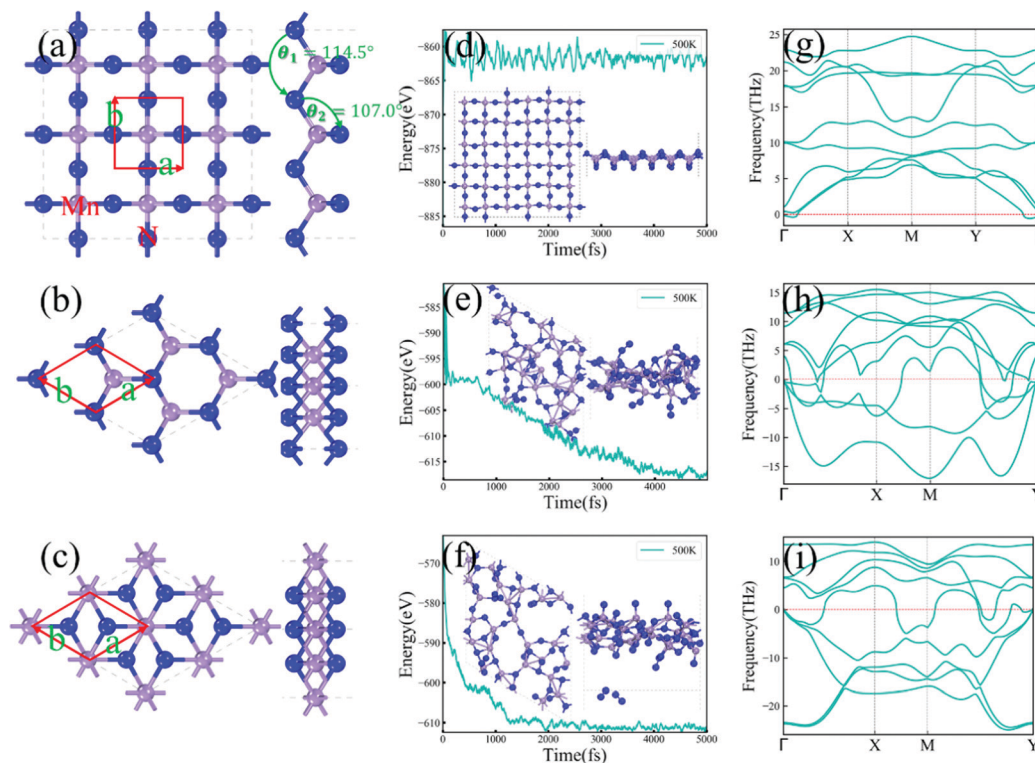


Fig. 1 (a–c) Atomic structures of the tetra-, h- and t-MnN₂ monolayers, respectively. The red boxes denote a primitive cell used for the calculation. (d–f) Variations in total energy versus time for the tetra-, h-, and t-MnN₂ monolayers in AIMD simulations at 500 K, respectively. Insets present the top and side views of snapshots at the end of AIMD simulations of 5 ps. (g–i) Phonon dispersion of the tetra-, h-, and t-MnN₂ monolayers, respectively.

to or larger than these results, which suggest that the tetra-TMN₂s could be energetically stable and feasible in the experiment.

Ab initio molecular dynamics (AIMD) simulations are performed to study the thermal stability of tetra-TMN₂s. The simulations are carried out by using a $5 \times 5 \times 1$ supercell at a temperature of 500 K for 5 picoseconds (ps) with a time step of 1 femtosecond (fs). In Fig. 1(d) we displayed the variations in total energy versus time for the tetra-MnN₂ monolayer during the entire simulations, and those for the other seven tetra-TMN₂s monolayers are shown in Fig. S2 (ESI[†]). From these pictures, we can see that, during the entire simulations, the total energies of tetra-TMN₂s fluctuate around a certain value which confirm that all these tetra-TMN₂s are thermally stable at 500 K. The AIMD results of h- and t-MnN₂ monolayers are displayed in Fig. 1(e and f), from which we can see that, in both cases, the total energy dramatically decreases and the structures are seriously disrupted, demonstrating that tetra-MnN₂ has better thermal stability than h- and t-MnN₂ monolayers. To further investigate the thermal properties of the tetra-MnN₂ monolayer, we increase the temperature to 700 K and 1000 K during the AIMD simulation, and we find that, as shown in Fig. S2(a and b) (ESI[†]), tetra-MnN₂ remains intact at 700 K, while at 1000 K the system collapses to a distorted configuration with formation of N₂ dimers, which shows that the tetra-MnN₂ monolayer has a melting point between 700 and 1000 K.

To confirm the dynamical stability of the tetra-TMN₂s monolayer, we calculated their phonon dispersions by using a

$5 \times 5 \times 1$ supercell and the results are presented in Fig. 1 and Fig. S3 (ESI[†]). There are no imaginary frequencies in the phonon dispersions for tetra-Tc/Re/OsN₂ and only negligible negative frequencies around the Γ point for tetra-Mn/Mo/Ru/W/IrN₂, which implied that tetra-TMN₂s are dynamically stable. As a comparison, in Fig. 1(h and i) the phonon dispersions of the h- and t-MnN₂ monolayers, respectively, are displayed, from which we can see that both of these structures are not dynamically stable due to the very tangible negative frequencies.

Properties of tetra-TMN₂

In Table S2 (ESI[†]), the elastic constants, Young's moduli and Poisson's ratios of tetra-TMN₂s and graphene are displayed. Our calculated values of graphene are well consistent with the results of a previous study,⁴³ demonstrating the validity of the methods used in this study. The elastic constants of tetra-TMN₂s satisfy the mechanical stability criteria⁴⁴ ($C_{11}, C_{22}, C_{66} > 0$ and $C_{11}, C_{22} - C_{12}^2 > 0$ for tetragonal 2D materials), indicating that tetra-TMN₂s are mechanically stable. As shown in Table S2 (ESI[†]), the Young's moduli of tetra-TMN₂s range from 72.4 (N m⁻¹) for tetra-IrN₂ to 129.2 (N m⁻¹) for tetra-TcN₂. These values are comparable to those of TiC₂ (131 N m⁻¹),⁴⁵ MoS₂ monolayer⁴⁶ (120.1 N m⁻¹), and penta-PdN₂⁴⁷ (127 N m⁻¹) and larger than those of germanene (42 N m⁻¹) and silicene (61 N m⁻¹).⁴⁸ In Fig. 2, we displayed the angular-dependent Young's modulus^{49,50} and Poisson's ratio of tetra-MnN₂. The Poisson's ratio of tetra-MnN₂ varies spatially with a minimum value of 0.15 along the x direction and a maximum value of

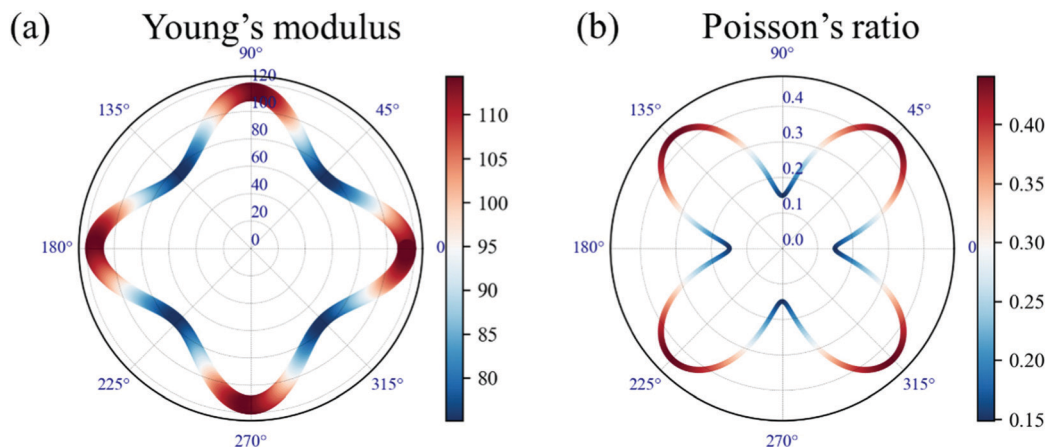


Fig. 2 (a) Angular-dependent Young's modulus (a) and Poisson's ratio (b).

0.44 along the diagonal direction, which is very similar to that of penta-Pt₂N₄.⁵¹ In addition, this deviation of Young's modulus and Poisson's ratio from the perfect circle clearly indicates the mechanical anisotropy, which can be understood from the fact that the Mn–N bonds are along the *x* and *y* directions in tetra-MnN₂.

In Fig. 3, the projected density of states (p-DOS) of each element, the 2p orbitals of N and the d orbitals of transition metal tetra-TMN₂s are displayed. Clearly, in all cases, the DOS around the Fermi level are mainly contributed by the N-2p and TM-d orbitals. There is a large overlap between the N-2p and TM-d states, suggesting a strong p–d hybridization. For the

Tc/Ru/Re/Os/Ir cases, there is no gap on the Fermi level, which makes them metallic, while for the Mo and W cases they are semiconducting with indirect band gaps of 1.38 eV and 1.96 eV (at the HSE06 level and their corresponding band structures are presented in Fig. S4(b and c), respectively, ESI†) for tetra-MoN₂ and tetra-WN₂, respectively. As shown in Fig. 4b and e, the occupied states near the Fermi level are mainly contributed by TM-d orbitals, while the N-2p states dominate the unoccupied states above the Fermi level. In fact, as indicated by the spatial distribution of electron density (shown in Fig. S5, ESI†), for the Mo and W cases, compared to the other six tetra-TMN₂s, the electrons are more localized around the N atoms, which

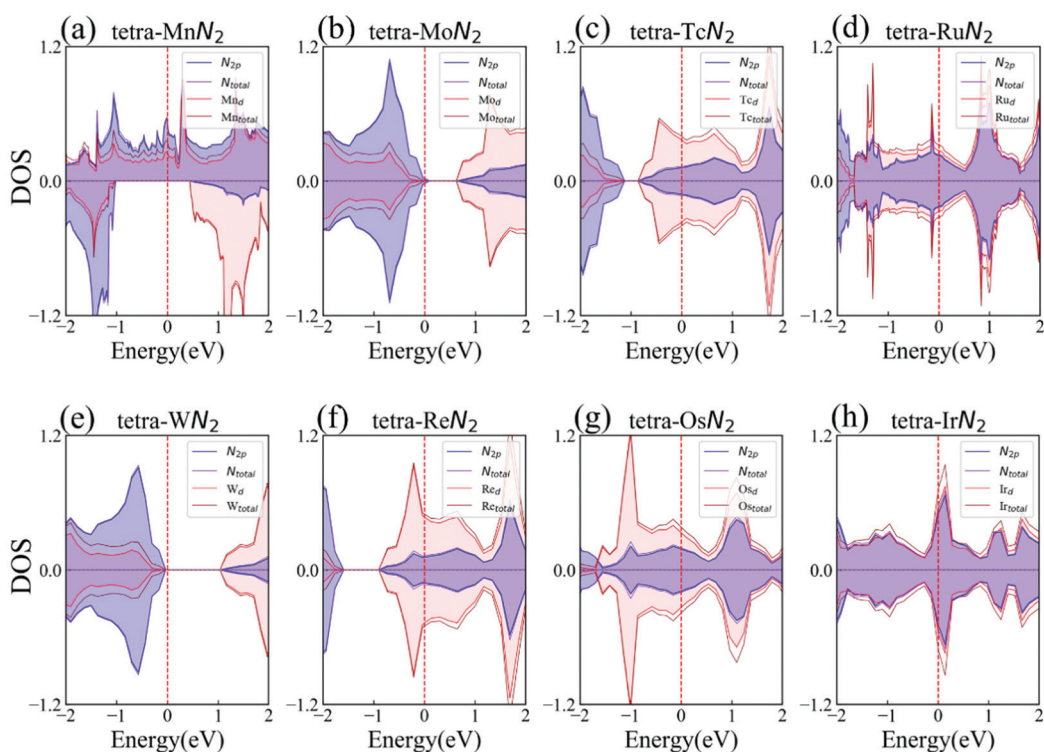


Fig. 3 Projected density of states (p-DOS) of tetra-TMN₂s. N-p and TM-d states are marked by light blue and red shadows, respectively.

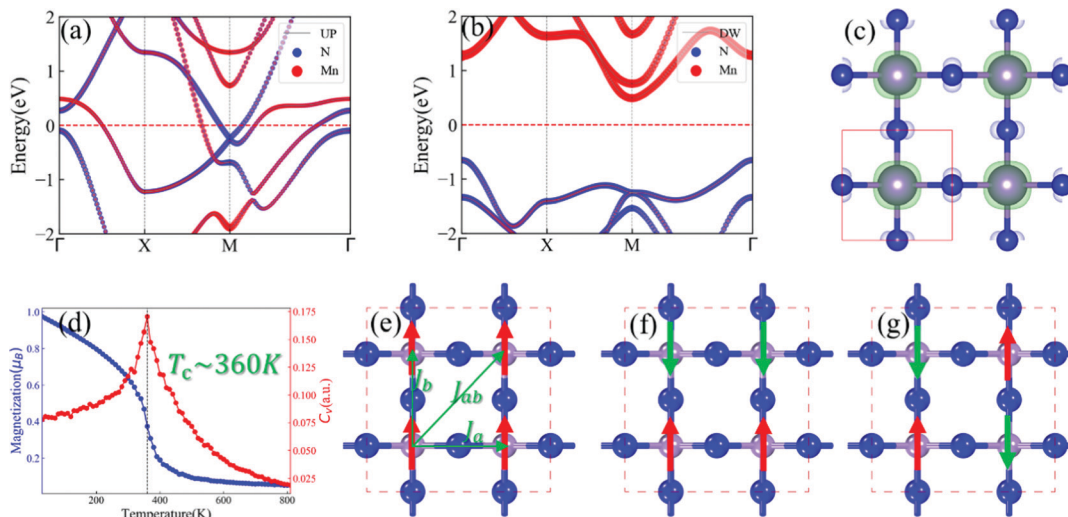


Fig. 4 (a) Spin-up and (b) spin-down projected band structures of tetra-MnN₂. (c) Spin-charge density ($\rho_{\uparrow} - \rho_{\downarrow}$) (isosurfaces = $0.04 e \text{ \AA}^{-3}$) of tetra-MnN₂, where shallow green and blue regions represent the positive and negative values, respectively. (d) Magnetic moment per unit and specific heat C_v of tetra-MnN₂ with respect to the temperature. Magnetic configurations of tetra-MnN₂: (e) FM, (f) AFM1, and (g) AFM2.

suggests that tetra-MoN₂ and WN₂ present stronger TM–N ionic bonding than the other six tetra-TMN₂s. This was further explained by Bader charge analysis,⁵² as displayed in Table 1; among all the tetra-TMN₂s, tetra-MoN₂ and WN₂ show the largest amounts of negative charges (-1.88 and $-2.16 e$ for tetra-MoN₂ and tetra-WN₂, respectively). Besides, an electron deficient region appeared around the TM atoms for the Mo and W cases, indicating that the Mo and W ions give all valence electrons to form ionic bonding with N ions. Therefore, the tetra-MoN₂ and tetra-WN₂ present semiconductor characteristics among all the tetra-TMN₂s.

Electronic and magnetic properties of tetra-MnN₂

Most intriguingly, tetra-MnN₂ exhibits a spin-polarization around the Fermi level, namely the spin-up states and spin-down states are not equivalent. Fig. 4(a and b) display the spin-resolved band structures for tetra-MnN₂. The spin-up bands cross the Fermi level, while the spin-down channel shows a band gap of 3.43 eV (at the HSE06 level and the corresponding band structures are presented in Fig. S4(a), ESI†). The valence and conduction bands around the Fermi level are dominated by N (marked by blue dots) and Mn (marked by red dots) ions, respectively. Due to this large band gap in the spin-down channel, the tetra-MnN₂ shows a 100% spin polarization ratio near the Fermi level. These make the tetra-MnN₂ a half-metal promising for spintronic devices.

To determine the magnetic ground state of tetra-MnN₂, as shown in Fig. 4(e–g), three possible magnetic configurations, including the ferromagnetic (FM) order and two different antiferromagnetic (AFM) orders, have been considered. Our results show that the total energy of the FM state is lower by 203.8 meV per unit cell than that of the AFM1 state and 240.6 meV than that of the AFM2 state, which indicates that tetra-MnN₂ has robust ferromagnetism. The strong ferromagnetic coupling in tetra-MnN₂ can be attributed to the strong super-exchange interaction between the

adjacent Mn ions mediated by N ions. In fact, as indicated by previous studies, the magnetic coupling between the Mn atoms in a Mn₂ dimer is antiferromagnetic, while it becomes ferromagnetic when a N atom is introduced.⁵³ As mentioned above, the reduction of the crystal field in such tetrahedral coordination in tetra-MnN₂ would enhance the super-exchange as the energy gap between the occupied and the empty spin-polarized Mn-d orbitals is reduced. Consequently, the ferromagnetic coupling in tetra-MnN₂ could be stronger than that in other Mn-based magnetic transition metal compounds such as the hexagonal MnN monolayer.⁵⁴ Fig. 4(c) displays the spin-charge density of tetra-MnN₂, which clearly shows that the spin-polarization is mainly contributed by the Mn ions, while the N ions are slightly spin-polarized with a tiny magnetic moment contrary to the Mn ions. This is very different from the case of h-MoN₂,²⁴ where the spin-polarization is dominated by the N-p orbitals and the ferromagnetism originates from the carrier-mediated direct interactions between N ions.

In addition, the magnetocrystalline anisotropy energies (MAEs) of the tetra-MnN₂ unit cell by including the effect of spin-orbit coupling (SOC) have also been calculated. Three magnetization directions, namely [100], [010] and [001] directions, are considered. Our results show that the MAE of the [001] direction is lower by 220 μeV per Mn atom than that of the [100] and [010] directions (these two magnetization directions have the same energy), indicating that the easy axis of the tetra-MnN₂ monolayer is along the [001] (out-of-plane) direction. This allows the formation of long-range 2D magnetic order according to the Mermin–Wagner theorem.⁵⁵

Finally, the Curie temperature (T_c) of tetra-MnN₂ is calculated by performing Monte Carlo (MC) simulation based on the Heisenberg model including the single-ion anisotropy. The Hamiltonian of the Heisenberg model is expressed as³¹

$$\hat{H} = - \sum_{\langle ij \rangle} J_{ij} \vec{S}_i \cdot \vec{S}_j - \sum_{\langle i \rangle} D(S_{iz})^2$$

where the summation $\langle ij \rangle$ runs over all the nearest-neighbor Mn sites, J_{ij} is the isotropic exchange interaction parameter (as illustrated in Fig. 4e), D is the single-ion magnetic anisotropy parameter, S_{iz} represent the components of S along z (out-of-plane) orientations and $|S|$ is set as $1/2$ for Mn ions since the magnetic moment on each Mn ion is $1 \mu_B$. The energies for each considered magnetic configuration in a $2 \times 2 \times 1$ supercell can be written as

$$E_{\text{FM}} = E_0 - (4J_a + 4J_b + 8J_{\text{ab}})S^2$$

$$E_{\text{AFM1}} = E_0 - (4J_a - 4J_b - 8J_{\text{ab}})S^2$$

$$E_{\text{AFM2}} = E_0 - (-4J_a - 4J_b + 8J_{\text{ab}})S^2$$

We obtain $J_a = J_b = 60.2$ meV because of the 4-fold rotation symmetry, $J_{\text{ab}} = 20.9$ meV. $D = 0.88$ meV is obtained from the SOC calculations. During the MC simulations, a 50×50 2D supercell is used to minimize the periodic constraints. The simulations are carried out for 8×10^5 loops at each temperature. In each loop, the spin at each site rotates randomly. The variations of the average magnetic moment per unit cell and the specific heat⁵⁶ (T_c) of tetra-MnN₂ are displayed in Fig. 4(d), from which T_c can be determined to be ~ 360 K, and this T_c value is above room temperature and is higher than those of recently reported 2D materials.^{57–60}

Finally, as a supplement, we also evaluated the stability and properties of the tetra-MnN₂ bilayer system (bi-tetra-MnN₂). Our results showed that, for bi-tetra-MnN₂, the AA-stacked configuration is more feasible and the thermal and dynamical stabilities are maintained. In addition, bi-tetra-MnN₂ exhibits ferromagnetic interlayer magnetic coupling and the half-metallicity is preserved (see the ESI† for more details).

Conclusion

In summary, based on density functional theory, we have used our custom code to systematically investigate all the 3d, 4d and 5d transition metal dinitride structures with h-, t- and tetra-phases. We find that (1) the tetra-phases of Mn, Mo, Tc, Ru, W, Re, Os and Ir dinitrides have a much lower energy compared to the h- and t-phases and all of them are dynamically, thermally and mechanically stable. (2) Their Young's moduli are comparable to that of the MoS₂ monolayer and larger than that of germanene. (3) Tetra-MoN₂ and tetra-WN₂ are non-magnetic semiconductors having indirect band gaps of 1.38 eV and 1.96 eV, respectively. (4) Tetra-TcN₂, RuN₂, ReN₂, OsN₂ and IrN₂ are intrinsic metals. (5) In particular, tetra-MnN₂ exhibits half-metallicity with a band-gap of 3.43 eV in the spin-down channel, a high Curie temperature of up to ~ 360 K and out-of-plane magnetic anisotropy, which make the tetra-MnN₂ monolayer a promising material for room-temperature nanoscale spintronic applications with high performance.

Conflicts of interest

There are no conflicts of interest to declare.

Acknowledgements

This work was supported by the NSFC (12004183, 11774173, 12074188), the Fundamental Research Funds for the Central Universities (No. 30921011214 and 30920041115), the Youth Program of NSF of Jiangsu Province (BK20200457), and the Hefei National Laboratory for Physical Sciences at the Micro-scale (KF2020104). C. H. and E. K. acknowledge the support from the Tianjing Supercomputer Centre and Shanghai Supercomputer Center.

Notes and references

- B. Huang, G. Clark, E. Navarro-Moratalla, D. R. Klein, R. Cheng, K. L. Seyler, D. Zhong, E. Schmidgall, M. A. McGuire, D. H. Cobden, W. Yao, D. Xiao, P. Jarillo-Herrero and X. Xu, *Nature*, 2017, **546**, 270–273.
- C. Gong, L. Li, Z. Li, H. Ji, A. Stern, Y. Xia, T. Cao, W. Bao, C. Wang, Y. Wang, Z. Q. Qiu, R. J. Cava, S. G. Louie, J. Xia and X. Zhang, *Nature*, 2017, **546**, 265–269.
- Y. J. Deng, Y. J. Yu, Y. C. Song, J. Z. Zhang, N. Z. Wang, Z. Y. Sun, Y. F. Yi, Y. Z. Wu, S. W. Wu, J. Y. Zhu, J. Wang, X. H. Chen and Y. B. Zhang, *Nature*, 2018, **563**, 94–99.
- Z. Fei, B. Huang, P. Malinowski, W. Wang, T. Song, J. Sanchez, W. Yao, D. Xiao, X. Zhu, A. F. May, W. Wu, D. H. Cobden, J.-H. Chu and X. Xu, *Nat. Mater.*, 2018, **17**, 778–782.
- I. Choudhuri, P. Bhauriyal and B. Pathak, *Chem. Mater.*, 2019, **31**, 8260–8285.
- Z. Sun, Y. Yi, T. Song, G. Clark, B. Huang, Y. Shan, S. Wu, D. Huang, C. Gao, Z. Chen, M. McGuire, T. Cao, D. Xiao, W. T. Liu, W. Yao, X. Xu and S. Wu, *Nature*, 2019, **572**, 497–501.
- W. Chen, Z. Sun, Z. Wang, L. Gu, X. Xu, S. Wu and C. Gao, *Science*, 2019, **366**, 983–987.
- X. Wang, J. Tang, X. Xia, C. He, J. Zhang, Y. Liu, C. Wan, C. Fang, C. Guo and W. Yang, *Sci. Adv.*, 2019, **5**, eaaw8904.
- T. Song, X. Cai, M. W.-Y. Tu, X. Zhang, B. Huang, N. P. Wilson, K. L. Seyler, L. Zhu, T. Taniguchi and K. Watanabe, *Science*, 2018, **360**, 1214–1218.
- M. Bonilla, S. Kolekar, Y. Ma, H. C. Diaz, V. Kalappattil, R. Das, T. Eggers, H. R. Gutierrez, P. Manh-Huong and M. Batzill, *Nat. Nanotechnol.*, 2018, **13**, 289–293.
- X. Sun, W. Li, X. Wang, Q. Sui, T. Zhang, Z. Wang, L. Liu, D. Li, S. Feng, S. Zhong, H. Wang, V. Bouchiat, M. Nunez Regueiro, N. Rougemaille, J. Coraux, A. Purbawati, A. Hadj-Azzem, Z. Wang, B. Dong, X. Wu, T. Yang, G. Yu, B. Wang, Z. Han, X. Han and Z. Zhang, *Nano Res.*, 2020, **13**, 3358–3363.
- K. Lee, A. H. Dismukes, E. J. Telford, R. A. Wisconsin, J. Wang, X. Xu, C. Nuckolls, C. R. Dean, X. Roy and X. Zhu, *Nano Lett.*, 2021, **21**, 3511–3517.

- 13 L. Liu, Z. Lin, J. Hu and X. Zhang, *Nanoscale*, 2021, **13**, 8137–8145.
- 14 S. Haastrup, M. Strange, M. Pandey, T. Deilmann, P. S. Schmidt, N. F. Hinsche, M. N. Gjerding, D. Torelli, P. M. Larsen, A. C. Riis-Jensen, J. Gath, K. W. Jacobsen, J. J. Mortensen, T. Olsen and K. S. Thygesen, *2D Mater.*, 2018, **5**.
- 15 M. Fukuda, J. Zhang, Y.-T. Lee and T. Ozaki, *Mater. Adv.*, 2021, **2**, 4392–4413.
- 16 S. M. Wang, H. Ge, S. L. Sun, J. Z. Zhang, F. M. Liu, X. D. Wen, X. H. Yu, L. P. Wang, Y. Zhang, H. W. Xu, J. C. Neufeind, Z. F. Qin, C. F. Chen, C. Q. Jin, Y. W. Li, D. W. He and Y. S. Zhao, *J. Am. Chem. Soc.*, 2015, **137**, 4815–4822.
- 17 C. Z. Zhang and Q. Sun, *J. Phys. Chem. Lett.*, 2016, **7**, 2664–2670.
- 18 S. Gong, C. Z. Zhang, S. Wang and Q. Wang, *J. Phys. Chem. C*, 2017, **121**, 10258–10264.
- 19 Y. Wang and Y. Ding, *J. Phys. Chem. C*, 2018, **122**, 26748–26755.
- 20 X. Guo, F. Li, Y. Zhu, X. Han and Y. Yan, *Appl. Phys. Lett.*, 2020, **116**, 113101.
- 21 M. K. Mohanta and A. De Sarkar, *Phys. Rev. B*, 2020, **102**, 125414.
- 22 M. K. Mohanta, I. S. Fathima and A. De Sarkar, *Phys. Chem. Chem. Phys.*, 2020, **22**, 21275–21287.
- 23 Y. Sun, B. Xu and L. Yi, *Chin. Phys. B*, 2020, **29**, 023102.
- 24 F. Wu, C. X. Huang, H. P. Wu, C. Lee, K. M. Deng, E. J. Kan and P. Jena, *Nano Lett.*, 2015, **15**, 8277–8281.
- 25 Y. Wang, S. S. Wang, Y. H. Lu, J. Z. Jiang and S. Y. A. Yang, *Nano Lett.*, 2016, **16**, 4576–4582.
- 26 Y. L. Wang and Y. Ding, *J. Mater. Chem. C*, 2016, **4**, 7485–7493.
- 27 C. Zhang, J. Liu, H. Shen, X.-Z. Li and Q. Sun, *Chem. Mater.*, 2017, **29**, 8588–8593.
- 28 H. P. Wu, Y. Qian, R. F. Lu and W. S. Tan, *Phys. Lett. A*, 2016, **380**, 768–772.
- 29 S.-H. Zhang and B.-G. Liu, *Nanotechnology*, 2018, **29**, 325401.
- 30 J. Xu, D. Wang, Y. Liu, R. Lian, X. Gao, G. Chen and Y. Wei, *J. Mater. Chem. A*, 2019, **7**, 26858–26866.
- 31 C. X. Huang, J. S. Feng, F. Wu, D. Ahmed, B. Huang, H. J. Xiang, K. M. Deng and E. J. Kan, *J. Am. Chem. Soc.*, 2018, **140**, 11519–11525.
- 32 G. Kresse and J. Furthmüller, *Comput. Mater. Sci.*, 1996, **6**, 15–50.
- 33 P. E. Blochl, *Phys. Rev. B: Condens. Matter Mater. Phys.*, 1994, **50**, 17953–17979.
- 34 J. P. Perdew, K. Burke and M. Ernzerhof, *Phys. Rev. Lett.*, 1996, **77**, 3865.
- 35 J. Heyd, G. E. Scuseria and M. Ernzerhof, *J. Chem. Phys.*, 2003, **118**, 8207–8215.
- 36 A. Togo and I. Tanaka, *Scr. Mater.*, 2015, **108**, 1–5.
- 37 V. Wang, N. Xu, J.-C. Liu, G. Tang and W.-T. Geng, *Comput. Phys. Commun.*, 2021, **267**, 108033.
- 38 J. D. Hunter, *Comput. Sci. Eng.*, 2007, **9**, 90–95.
- 39 K. Momma and F. Izumi, *J. Appl. Crystallogr.*, 2011, **44**, 1272–1276.
- 40 M. Qiao, Y. Wang, Y. F. Li and Z. F. Chen, *J. Phys. Chem. C*, 2017, **121**, 9627–9633.
- 41 Y. Zhang, Z. F. Wu, P. F. Gao, D. Q. Fang, E. H. Zhang and S. L. Zhang, *Phys. Chem. Chem. Phys.*, 2017, **19**, 2245–2251.
- 42 C. Ataca, M. Topsakal, E. Akturk and S. Ciraci, *J. Phys. Chem. C*, 2011, **115**, 16354–16361.
- 43 R. C. Andrew, R. E. Mapasha, A. M. Ukpogon and N. Chetty, *Phys. Rev. B: Condens. Matter Mater. Phys.*, 2012, **85**, 125428.
- 44 J. Wang, S. Yip, S. R. Phillpot and D. Wolf, *Phys. Rev. Lett.*, 1993, **71**, 4182–4185.
- 45 T. Zhao, S. Zhang, Y. Guo and Q. Wang, *Nanoscale*, 2016, **8**, 233–242.
- 46 Q. Peng and S. De, *Phys. Chem. Chem. Phys.*, 2013, **15**, 19427–19437.
- 47 K. X. Zhao, X. Y. Li, S. Wang and Q. Wang, *Phys. Chem. Chem. Phys.*, 2019, **21**, 246–251.
- 48 R. John and B. Merlin, *Cryst. Struct. Theory Appl.*, 2016, **5**, 43–55.
- 49 E. Cadelano, P. L. Palla, S. Giordano and L. Colombo, *Phys. Rev. B: Condens. Matter Mater. Phys.*, 2010, **82**, 235414.
- 50 V. Wang and W. T. Geng, *J. Phys. Chem. C*, 2017, **121**, 10224–10232.
- 51 Z. Liu, H. D. Wang, J. Y. Sun, R. J. Sun, Z. F. Wang and J. L. Yang, *Nanoscale*, 2018, **10**, 16169–16177.
- 52 R. F. Bader, *Atoms in molecules*, Wiley Online Library, 1990.
- 53 B. K. Rao and P. Jena, *Phys. Rev. Lett.*, 2002, **89**, 4.
- 54 Z. M. Xu and H. Zhu, *J. Phys. Chem. C*, 2018, **122**, 14918–14927.
- 55 N. D. Mermin and H. Wagner, *Phys. Rev. Lett.*, 1966, **17**, 1133–1136.
- 56 K. Sato, L. Bergqvist, J. Kudrnovsky, P. H. Dederichs, O. Eriksson, I. Turek, B. Sanyal, G. Bouzerar, H. Katayama-Yoshida, V. A. Dinh, T. Fukushima, H. Kizaki and R. Zeller, *Rev. Mod. Phys.*, 2010, **82**, 1633–1690.
- 57 J. Y. Zhang, W. Xue and X. Y. Chen, *Nanotechnology*, 2020, **31**, 275301.
- 58 B. Huang, G. Clark, E. Navarro-Moratalla, D. R. Klein, R. Cheng, K. L. Seyler, D. Zhong, E. Schmidgall, M. A. McGuire, D. H. Cobden, W. Yao, D. Xiao, P. Jarillo-Herrero and X. D. Xu, *Nature*, 2017, **546**, 270–273.
- 59 C. Gong, L. Li, Z. L. Li, H. W. Ji, A. Stern, Y. Xia, T. Cao, W. Bao, C. Z. Wang, Y. A. Wang, Z. Q. Qiu, R. J. Cava, S. G. Louie, J. Xia and X. Zhang, *Nature*, 2017, **546**, 265–269.
- 60 M. Kan, J. Zhou, Q. Sun, Y. Kawazoe and P. Jena, *J. Phys. Chem. Lett.*, 2013, **4**, 3382–3386.